Harnessing thermoelectric power from transient heat sources:
Waste heat recovery from silicon production

Isha Savani[a], Magnus H. Waage[b], Marit Børset[c], Signe Kjelstrup[b], Øivind Wilhelmsen[d,e]

[a]Department of Physics, Norwegian University of Science and Technology, NTNU, Trondheim, Norway
[b]Department of Chemistry, Norwegian University of Science and Technology, NTNU, Trondheim, Norway
[c]Primary Metal Technology, Hydro Aluminium AS, NO-6885 Øvre Årdal, Norway
[d]Department of Electrical Engineering and Renewable Energy, Norwegian University of Science and Technology, NTNU, Trondheim, Norway
[e]SINTEF Energy Research, N-7465 Trondheim, Norway

Abstract

Thermoelectric generators (TEGs) are compact and robust devices for converting heat into electrical power. In this work, we investigate the response of a bismuth-telluride based TEG to the transient environment of a silicon production plant, where there is a periodic change in the average temperature of the heat source. We establish a dynamic mathematical model that reproduces results from industrial, on site experiments, both at steady-state and under transient conditions. By simultaneously changing the design and location of the TEG, a peak power density of 1971 W/m^2 can be obtained without exceeding material constraints of the TEG, with an average power density of 146 W/m^2. In the transient case, the average power density generated during one silicon casting cycle is in all investigated cases found to be only 7 - 10% of the peak power density as the peak value of the power is only maintained for a couple of minutes. The fractional area is defined as the ratio of the total area of thermoelectric modules to the total system cross-sectional area of the TEG. We find that the power generated can be increased by reducing the fractional area, provided that the TEG is at a fixed position. If the TEG can be placed as close as possible to the heat source without exceeding the material constraints, the peak power density and the average power density reach maximum values as functions of the fractional area, beyond which the power begins to decline. The optimal fractional area that gives maximum power depends strongly on the cooling capacity. We find that with a higher cooling capacity, it is beneficial to design the TEG with a higher fractional area and place it as close as possible to the silicon melt. Possible venues to improve the performance of TEGs that operate under transient conditions are suggested.

1. Introduction

As the world's natural resources deplete, making the best use of resources that go to waste is an important issue. The problem persists in all areas of production and consumption, and is met with in diverse ways, for instance by designing materials that help rehabilitate derelict buildings [1] or by capturing and reusing carbon-dioxide and methane from landfills [2]. Furthermore, to meet the energy requirements of a growing and insatiable society, a large portion of methods for harvesting power rely on novel devices like solar cells, wind turbines, photovoltaic cells and thermoelectric generators (TEGs) [3]. Recently, TEGs are being integrated with photovoltaic cells to enhance power output [4].

A TEG is a device which is durable, easily scalable and does not require much maintenance [3]. This device operates on the principle of producing electrical energy from a temperature difference. There is a large potential to enhance the heat conversion efficiency of TEGs and to increase the power output by manipulating their design [5, 6], or by introducing new materials. The efficiency of a TEG depends on many aspects of its design, such as the density of p/n modules, the nature of electrical load connected to the TEG and the ratio of length of individual layers to the cross sectional area [7]. In addition, the cost of the device due to the expensive rare earth metals that are used, can be lowered by reducing the fraction of the cross-sectional area in the thermoelectric module (TEM) that contains active material, in addition to reducing the thickness of the metal conductors [8, 9].

Several studies presented in the literature have explored the potential of TEGs by combining theory and laboratory experiments [10–13]. A lot of work has also been done with regards to mathematical modeling and simulations [14–17]. A three-dimensional model of a TEG was developed by Shi et al. [18], where the performance of the TEG was evaluated under changes in height, cross-sectional area, and number of TEG pairs.

Thermoelectric power generation at the very site of its practical application provides a robust evaluation of these devices. To name a few practical sites; in space, (radioactive) TEGs are used to power the International space station, and in the sea, waste heat from incinerators on a ship have been used to harvest energy [19]. Thermoelectric generators have also been tested for use inside the engines of Chevrolet suburban cars [20].

Email address: `isha.savani@gmail.com` (Isha Savani)

Most of the studies presented in the literature have evaluated the performance of TEGs at or close to steady-state conditions, while a few previous works have considered transient aspects. Driving conditions of vehicles affect the performance of TEGs; Yu et al. [21] have looked at the varying response of TEGs under acceleration and deceleration which affect the hot-side temperature of the TEG. Nguyen et al. [22] considered the time evolution of the temperature of the hot plate of the TEG while taking into account the Thomson effect. Montecucco et al. [23, 24] looked at the effect of a time change in DC electrical power and the current set in the electrical load. Transients, such as periodically oscillating temperature gradients [25], or varying both hot and cold source temperatures [26, 27], also provide a testing ground for the efficiency of TEGs. In all these cases, the physical process involved in thermoelectric power generation and the power harnessed from such processes are shown to vary with time. Under varying thermal loads, there is a time change in the temperature gradient over the TEG. Paraskevas et al. [28] have looked at a maximum power point tracking method to find how the power produced by the TEG source can be maximized.

So far, there has not been done enough research on implementing TEGs in industrial settings. This represents a rather unexploited opportunity for converting excess heat into electrical power. To our knowledge, the first study combining mathematical modeling with on-site measurements in the metal industry is very recent. Kuroki et al. obtained a power density as high as ~1 kW/m^2, by exploiting bismuth-telluride thermoelectric generation modules in a steel making process (See Fig. 9 in Ref. [29]). More recently, Chen et al. studied the efficiency of TEGs under a pulsed power source in iron and steel factories [30]. Many industrial processes are highly dynamic. For instance, in the silicon production process recently investigated by Børset et al. [31], metal is cast in batches. In such processes, the expected potential for the average power output density is likely to be significantly below 1 kW/m^2. In this work, we address the important questions: How much power can realistically be extracted from such processes? What is the optimal design of the TEG constructed to maximize the time-average power density under highly dynamic operation conditions?

To address these questions, we have developed a transient mathematical model for heat and charge transport in a TEG, placed in the casting area of a silicon production plant. We will compare the model to on-site measurements made under dynamic operating conditions and will determine the maximum, average power that can be extracted from the silicon casting process. Moreover, we discuss how TEGs can be optimally designed in order to achieve this goal. These questions have, to the best of our knowledge, not been addressed before in the literature. We have used bismuth-telluride based thermoelectric modules (TEMs), but modules made from other materials are expected to behave similarly. Besides being relevant to many similar industrial facilities involving the production of silicon, the conclusions we draw in this work will be relevant to the metal casting industry in general.

Figure 1: The silicon casting area. A ladle full of molten silicon is poured into trays, one by one as the trays rotate on the carousel.

2. Description of the TEG and its environment

The amount of power that can be harnessed by a TEG depends on both its design and the heat source that is exploited to generate electrical power. In this section, we provide specifications of the design of an in-house TEG construction, and the casting facility at the silicon production plant, Elkem Salten, in Norway, where the TEG has been tested. The TEG design and the silicon casting facility were described in detail in Ref. [31] and only the essential elements are repeated here.

2.1. Silicon casting facility

In the process of silicon production, molten silicon at 1723 K is cast into ladles moving on a conveyor belt, called *casting carousel*, as illustrated in Fig. 1. The ladle has 8000-9000 kg of silicon and it takes about 20-25 minutes to empty the ladle completely into several molds. The casting process is repeated once every two hours. Since the melting point of silicon is 1683 K, the casting area maintains a high temperature for a long time before the silicon solidifies, this provides an ideal environment for converting excess heat to electrical power.

On one side of the casting area, a wall is placed to screen the intense radiation from the silicon melt. The TEG is placed in a little window carved out in the wall. The horizontal distance of the TEG from the outer ring of the casting carousel is 0.7 m.

2.2. TEG design

The TEG consists of TEMs arranged in a 6×6 grid; 6 modules are connected in series, and 6 series are connected in parallel. The TEMs used this work was the TEP-1264-1.5 model by Thermonamic, China. These modules have been well characterized in the literature, where details about properties and manufacturing are available at the supplier's webpage. Each module consists of 126 pairs of p/n semiconductors connected in series with an external resistance. The module area is 40×40 mm^2. Figure 2 shows the arrangement of the modules in a grid. On either side of a module, a ceramic layer of aluminum-oxide is placed next to a thin layer of copper. The arrangement of TEMs shown in Fig. 2, is placed between hot and cold plates of aluminum. The total surface area of the TEG is 0.5×0.5 m^2. On
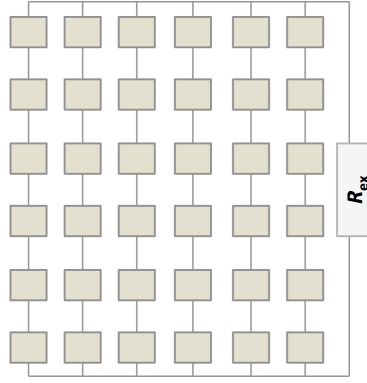
Figure 2: The grid of TEMs connected to an external resistance R_{ex} in series. Each module contains 126 pairs of p/n semiconductors [31].
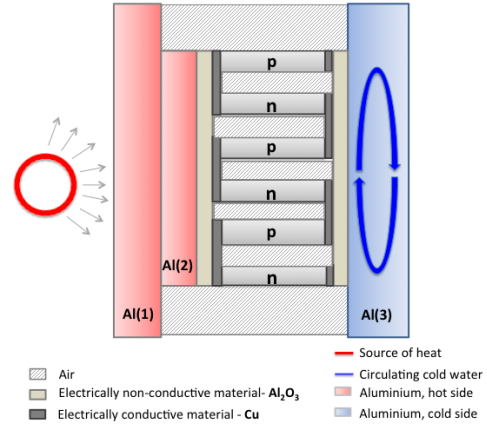

Figure 4: The cross section of a TEG unit, where the heat source and the heat sink are illustrated. Cold water runs through copper pipes that are mounted at the last aluminum layer (to the right). The unit consists of eight layers, three aluminum segments, two segments made from Al_2O_3 + Cu, one segment constituting p/n semiconductors, and two regions where air is in contact with the device

one side of the generator, aluminum is directly exposed to radiation from the silicon melt (aluminum hot side). On the other side, the aluminum plate is in contact with cold water maintained at a temperature of 279 K, circulating in copper pipes embedded in the plate (aluminum cold side). Tap water is used for cooling. The surrounding air temperature is 288 K.

In the mathematical model, the whole TEG will be divided into $N_p \times N_s = 36$ **units**, where N_s and N_p are the number of units connected in series and number of series connected in parallel. It is only necessary to model one of these units since they are equivalent in all respects. Figure 3 shows how the units form the TEG. We emphasize that *the unit* is only a theoretical construct and that the aluminum plates at the back and the front of the TEG are continuous.
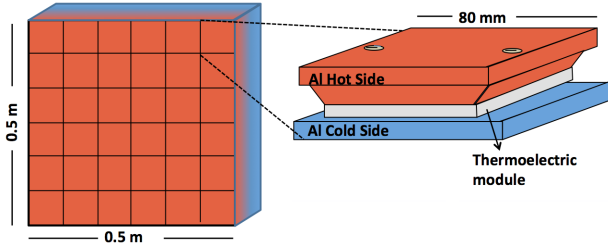

Figure 3: The TEG (left) and one thermoelectric unit (right). One unit consists of a TEM placed in between aluminum hot side and cold side [31]. Each TEM contains 126 pairs of p/n semiconductors.

One thermoelectric unit is 80×80 mm^2. Each unit is also in contact with several layers of air. One layer is located in between each semi-conductor pair, and one layer runs parallel to the other layers at both ends of a module. The cross section of a thermoelectric unit is illustrated in Fig. 4.

3. Governing equations

In this section, we state the main equations that govern heat and charge transfer through the TEG. We will also establish a mathematical model of the silicon casting process which is the transient heat source for the TEG.

3.1. Temperature gradient through the TEG

In order to establish an analytical expression for the time change in temperature through the TEG, we begin with the energy balance equation. The energy balance relates the rate of change in the internal energy density, u, of a system, or the change in temperature T of a system in time t, to fluxes entering or leaving a system,

$$\frac{\partial u(x,t)}{\partial t} = \rho c_p \frac{\partial T(x,t)}{\partial t} = -\frac{\partial J'_q(x,t)}{\partial x} - \frac{\partial \phi(x,t)}{\partial x} j. \quad (1)$$

The fluxes in question are the measurable heat flux $J'_q(x,t)$ and the electrical flux j, which are related to the transport of heat and charge respectively, ρ is the density of the material, c_p is the specific heat capacity and ϕ is the electrochemical potential of the the charge carrying species; the difference in ϕ gives the measured electric potential gradient. The last term on the right hand side of Eq. 1, with the sign convention used, refers to the power applied to the volume element in question. When heat is converted to electric power, it represents the power output.

In the presence of a temperature gradient, the coupling between heat and charge transport gives rise to a potential gradient. The gradients in temperature and potential are defined using the formalism developed in irreversible thermodynamics [32]. By starting with linear force-flux relations and identifying transfer coefficients, one arrives at

$$J'_q = -\lambda \frac{dT}{dx} + \frac{S^*T}{F} j, \quad (2)$$

$$j = -\frac{S^*}{Fr} \frac{dT}{dx} - \frac{1}{r} \frac{d\phi}{dx}. \quad (3)$$

Here, S^* is the transported entropy which is a kinetic property of charge carriers, λ is the thermal conductivity, F is the

Faraday constant and r is the electrical resistivity of the mate-[195]rial. Using Eqs. (2) and (3) together with the energy balance[196] (Eq. (1)), the time rate of change of temperature in layer i of the[197] TEG (see Fig. 4), is found to be[198]

$$\rho_i c_{p_i} \frac{\partial T(x,t)}{\partial t} = \lambda_i \frac{\partial^2 T(x,t)}{\partial x^2} + r_i j_i^2. \tag{4}$$

[174] Since current only flows through the layer constituting the p/n [175] semiconductors, $j = 0$ for the other layers.

3.1.1. Current generated in the transient case

The power P generated by the TEG is given by

$$P = R_{ex}I_{ex}^2 = \Delta\phi_{tot}I_{ex}, \tag{5}$$

where R_{ex} is the external resistance, I_{ex} is the current generated in the external circuit, and the terminal voltage is $\Delta\phi_{tot}$. The[202] external current is related to the current generated in each row[203] (series) of modules, I_s, by $I_{ex} = N_p I_s$, where N_p is the number of[204] series connected in parallel (see Fig. 2). The terminal voltage,[205] $\Delta\phi_{tot}$, is the total voltage of the thermoelectric generator. It is[206] related to the voltage of one TEM, $\Delta\phi_{mod}$ by $\Delta\phi_{tot} = N_s\Delta\phi_{mod}$. The electric potential gradient over a module, $\Delta\phi_{mod}$, is given by Eq. (3). Using the fact that the temperature difference across the semi-conductor is $\Delta T = T_h - T_c$, and that the current flows in opposite directions in the p- and n-type semiconductors, Eq. (3) is integrated to find the electric potential difference across one module[207]

$$\Delta\phi_{mod} = N_{pn}\left(\frac{S_p^* - S_n^*}{F}\right)(T_h - T_c) - N_{pn}\left(\frac{l_p r_p}{A_p} + \frac{l_n r_n}{A_n}\right)I_s. \tag{6}$$

[177] Here $l_p = l_n$ is the length, $A_p = A_n$ is the cross-sectional area and[211] [178] $r_p = r_n$ is the resistivity of the p and n semi-conductor respec-[212] [179] tively. Identifying the Seebeck coefficient, $\alpha = \frac{S_p^* - S_n^*}{F}$ and using[213] [180] Eq. (5), the current through the TEG is found to be[214]

$$I_s = \frac{N_{pn}N_s\alpha(T_h - T_c)}{N_p R_{ex} + N_{pn}N_s\left(r_n l_n/A_n + r_p l_p/A_p\right)}, \tag{7}$$

[181] where $N_{pn} = 126$, is the total number of pairs of p/n semi-[182] conductors connected electrically in series with copper strips [183] placed next to aluminum oxide layers in one module.

3.1.2. Heat flow equations through the TEG

[185] There are well defined interfaces between each layer that the[219] [186] TEG consists of. This is illustrated in Fig. 5. Since the inter-[220] [187] faces are very thin, they have very little capacity to store energy.[221] [188] Consequently, the dynamic responses in an interface are much [189] faster than in the bulk of the material. For the time-scales we [190] are interested in, it is safe to assume that the interfaces between [191] the layers have no capacitance, implying that the heat flow into [192] an interface equals the heat flow leaving it at all times. The [193] heat flow, $\dot{Q}$, is related to the heat flux by $\dot{Q} = AJ_q'$, where [194] A is the area of the surface under consideration. In this work,

we have neglected the resistance of the interfaces themselves, which is discussed extensively in other works [33–37]. This is a valid assumption, since soft graphite sheets with a very high thermal conductivity have been used as thermal interface material between the TEMs and the aluminum plates to ensure a low thermal resistance, and thus a low thermal contact resistance.
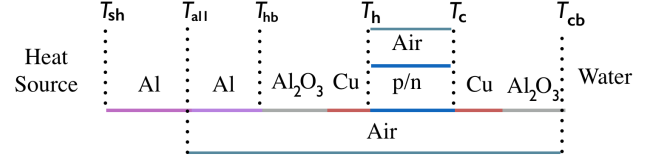

Figure 5: One-dimensional representation of the thermoelectric unit. The dotted lines represent the interfaces between each segment. The associated interfacial temperature is indicated at the top of each dotted line.

Due to the symmetry of the system, it is only necessary to model one of the units of the TEG since they are equivalent in all respects (see Fig. 3). The result is then multiplied by the appropriate factor to obtain the behavior for the whole system.

By taking into account heat transfer due to radiation and convection, the incoming heat flow at the aluminum hot side of the TEG is

$$\dot{Q}^{in} = N_p N_s A_{Al}\left(c_{rad}\sigma_B(T_m^4 - T_{sh}^4) + h_{wh}(T_{surr,h} - T_{sh})\right). \tag{8}$$

Here, $N_s = N_m = 6$, is the number of modules connect in series and number of series connected in parallel, $A_{Al} = 0.0069$ m^2 is the area of the aluminum plate of one unit, σ_B is the Stefan-Boltzmann constant and T_m, is the temperature of the molten silicon and $T_{surr,h} = 288$ K, is the surrounding air temperature. The parameter c_{rad} encapsulates the radiation view factor, the emissivity of the TEG surface, and also takes into account the radiation that gets absorbed by dust particles on its path to the TEG. The convective heat transfer coefficient from the aluminum hot side to surrounding air is h_{wh}.

The cold side of the TEG is in contact with water maintained at 279 K, circulating in pipes embedded in the the aluminum cold side. The transfer of heat across the last interface is due to convection only, and is given by

$$\dot{Q}^{out} = N_p N_s A_{Al} h_{cw}(T_{cb} - T_{cw}), \tag{9}$$

where T_{cw} is the temperature of the cold water, the convective heat transfer coefficient from the cold aluminum block to water is h_{cw} and T_{cb} is the temperature of the walls of the pipes in which water flows, which has here been assumed to be equal to the interface of the last aluminum segment.

Except for the p/n semiconductors, there is no transport of charge, so the transport of thermal energy is by conduction only. The transfer of heat through an electrically neutral layer i is given by Fourier's law

$$\dot{Q}_i = -N_p N_s \lambda_i A_i \frac{\partial T_i}{\partial x_i}. \tag{10}$$

4

In the p/n semiconductors, the current serves as an additional venue for transporting energy. Using Eq. (2) and summing over the heat flux through one of the p and n segments, one arrives at

$$\sum_{i=\mathrm{p,n}} J'_{q,i} = -\left(\lambda_{\mathrm{p}} + \lambda_{\mathrm{n}}\right)\frac{dT}{dx} + (S^*_{\mathrm{p}} - S^*_{\mathrm{n}})T\frac{j}{F}, \qquad (11)$$

where the fact that the current in the p/n segments flows in opposite directions is the reason why the transported entropies, S^*_{p} and S^*_{n} have opposite signs. Since $\lambda_{\mathrm{p}} = \lambda_{\mathrm{n}} = \lambda_{\mathrm{p/n}}$, and $A_{\mathrm{p}} = A_{\mathrm{n}} = A_{\mathrm{p/n}}$, and by using $j = I_{\mathrm{s}}/A_{\mathrm{p/n}}$ one arrives at

$$\sum_{i=\mathrm{p,n}} J'_{q,i} = -2\lambda_{\mathrm{p/n}}\frac{dT}{dx} + \alpha T\frac{I_{\mathrm{s}}}{A}. \qquad (12)$$

The heat flow through the $p + n$ segment is found to be

$$\sum_{i=\mathrm{p,n}} \dot{Q}_i = -2A_{\mathrm{p/n}}\lambda_{\mathrm{p/n}}\frac{dT}{dx} + \alpha T I_{\mathrm{s}}. \qquad (13)$$

In cases where the thermal conductivity of the p and n segments are different, Eq. 11 should be used instead.

3.2. Silicon casting process

In the casting process explained in Section 2.1, molten silicon is cast from a ladle onto a tray moving on a carousel. It takes about 20-30 minutes to empty a ladle into the molds. In the model, we have assumed that the silicon is fully loaded after 30 minutes. From on-site measurements, the average temperature on the hot side of the TEG is known. Casting occurs once every two hours [31]. We considered the source of heat and radiation to be the entire casting carousel, and we modeled the time change in source temperature by taking into account convective and radiative heat transfer. The process was modeled by the following equations

$$\frac{dT_{\mathrm{m}}(t)}{dt} = \begin{cases} a, & \text{for} \quad t < 30 \text{ mins} \\ \\ k_1(T^4_{\mathrm{m}}(t) - T^4_{\mathrm{surr,h}}) \\ +k_2(T_{\mathrm{m}}(t) - T_{\mathrm{surr,h}}) & \text{for} \quad t \geq 30 \text{ mins}, \end{cases} \qquad (14)$$

where T_{m} is the average temperature of the heat source. The first half of Eq. (14) is meant to represent gradual loading of silicon into the carousel. This is reflected in a linear increase in temperature over time, where the slope a, is chosen such that $T_{\mathrm{m}}(30 \text{ mins}) = 1673$ K, which is the melting point of silicon. The second half represents cooling by radiation and convection. Here,

$$k_1 = -\sigma_{\mathrm{B}}\epsilon_{\mathrm{s}}f/c'_{\mathrm{p}}, \qquad (15)$$

$$k_2 = -h_{\mathrm{wh}}f/c'_{\mathrm{p}}, \qquad (16)$$

where f is a fitting parameter that has units m^2 and is related to the area of the casting carousel, $\sigma_{\mathrm{B}} = 5.67 \times 10^{-8}$ Wm^{-2}K^{-4}

is the Stefan Boltzmann constant, $\epsilon_{\mathrm{s}} = 0.18$, is the emissivity of silicon taken from Ref. [38], $h_{\mathrm{wh}} = 6$ Wm^{-2}K^{-1} [31] is the convective heat transfer coefficient between air and aluminum, and c'_{p} with the units J/K, is the total heat capacity of approximately 9000 kg solid silicon [39].

Another fitting parameter is c_{rad}. In the transient case, we estimated the values $c_{\mathrm{rad}} = 0.036$ and $f = 200$ m^2. Details on how to estimate c_{rad} were provided in Ref. [31], while f wwas determined by matching the temperature at the hot-side of the TEG with experimental results, where several casting cycles where considered. We found that the magnitude of f influenced mainly the peak temperature of the hot-side temperature of the TEG, which could be matched well with experimental data. While k_1 and k_2 represent the rate of heating and cooling of the silicon melt, c_{rad} incorporates the location of the TEG with respect to the silicon melt into the model. Using the values above, we obtained $k_1 = 3.2\times10^{-16}$ 1/K^{3}s, and $k_2 = 1.9\times10^{-7}$ s^{-1}.

4. Numerical model

4.1. Modeling the TEG

Figure 4 shows the cross section of one unit of the TEG. It consists of eight layers- three aluminum segments, two segments made from Al$_2$O$_3$ + Cu, one segment constituting p/n semiconductors, and two regions where air is in contact with the device. There are well defined interfaces between each layer which are illustrated in Fig. 5. Cold water is flowing through copper pipes embedded in the last aluminum layer, so this layer is not included in the numerical modeling. The total length L of the system is then the sum of the length of seven layers, not including the last aluminum layer, given in Table 1.

The system is discretized and grid points are allotted to each segment depending on its length. The aluminum layers consist of 15 grid points, (Al$_2$O$_3$+Cu) consist of 7 and p/n consist of 20 grid points. The layer of air which is parallel to these layers consists of a total of (15+7+20) grid points. The layer in between p/n has 20 grid points allotted to it. The grid size was decided so that the simulation completes in a reasonable amount of time, without significant loss of accuracy. This was tested by increasing the grid size by 10 times of the reported values. With a 10 times denser grid, the temperatures during the transient evolution towards steady-state as well as the steady-state temperatures changed by less than 1 K.

We begin by establishing the heat flow into and out of each interface. Since the temperature profile in the bulk of the system in the transient case is not perfectly linear, the heat flow into a layer is not necessarily the same as the heat flow out of it. The heat flow into an interface is defined as $\dot{Q}^{\mathrm{in}}_i$ and the heat flow leaving an interface is defined as $\dot{Q}^{\mathrm{out}}_i$. The heat flows are illustrated in Fig. 6. As an example, the total heat flow across the interface between Al(2) and Al$_2$O$_3$ is given by

$$\dot{Q}_{\text{Al}(2)}^{\text{in}} = -N_{\text{p}}N_{\text{s}}A_{\text{Al}}\lambda_{\text{Al}}\frac{\Delta\text{T}_{l,\text{hb}}}{\Delta\text{x}_{l,\text{hb}}}, \tag{17}$$

$$\dot{Q}_{\text{Al}_2\text{O}_3}^{\text{out}} = -N_{\text{p}}N_{\text{s}}A_{\text{Al}_2\text{O}_3}\lambda_{\text{Al}_2\text{O}_3}\frac{\Delta\text{T}_{r,\text{hb}}}{\Delta\text{x}_{r,\text{hb}}}.$$

This is the Fourier-type of heat flow that was introduced in Eq. (10). Here $\Delta\text{x}_{l,\text{hb}}$ and $\Delta\text{x}_{r,\text{hb}}$, as indicated in Fig. 6, represent the distance between grid points in the immediate vicinity of the interface. $\Delta\text{T}_{l,\text{hb}}$ and $\Delta\text{T}_{r,\text{hb}}$ are the corresponding temperatures differences at those grid points.

The heat flow is proportional to the respective areas of the aluminum plate and the aluminum oxide plate in one unit of the TEG, A_{Al} and $A_{\text{Al}_2\text{O}_3}$, and the respective thermal conductivities λ_{Al} and $\lambda_{\text{Al}_2\text{O}_3}$. To obtain the total heat flow through the TEG, Eq. (17) has been multiplied by the total number of modules which is equal to $N_{\text{p}} \times N_{\text{s}}$. The interface temperature T_{hb} is such that $\dot{Q}_{\text{Al}(2)}^{\text{in}} = \dot{Q}_{\text{Al}_2\text{O}_3}^{\text{out}}$, ensuring that there is no accumulation of energy at the interface between the two layers.
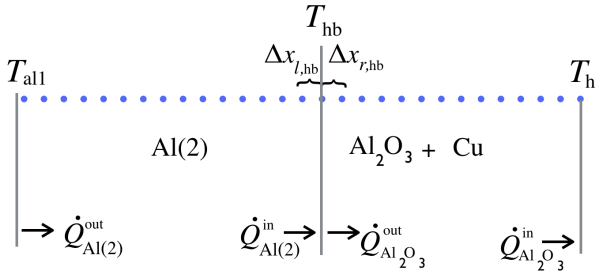

Figure 6: Illustrating heat flows $\dot{Q}^{\text{in/out}}$, entering and leaving the layers Al(2) and Al$_2$O$_3$ + Cu. The interfacial temperature between the two layers is T_{hb}.

In the p/n semiconductors, the current serves as an additional venue for transporting energy. Thus across the interface between the p/n semiconductors, energy balance takes into account a Fourier-type heat flow, and a heat flow contribution due to the current, (see Eq. (13)). The total heat flow through the TEMs is given by

$$\dot{Q}_{\text{pn}}^{\text{out}} = N_{\text{p}}N_{\text{s}}\left(-2N_{\text{pn}}A_{\text{p/n}}\lambda_{\text{p/n}}\frac{\Delta\text{T}_{r,\text{h}}}{\Delta\text{x}_{r,\text{h}}} + N_{\text{pn}}\alpha T_{\text{h}}I_{\text{s}}\right), \tag{18}$$

$$\dot{Q}_{\text{pn}}^{\text{in}} = N_{\text{p}}N_{\text{s}}\left(-2N_{\text{pn}}A_{\text{p/n}}\lambda_{\text{p/n}}\frac{\Delta\text{T}_{l,\text{c}}}{\Delta\text{x}_{l,\text{c}}} + N_{\text{pn}}\alpha T_{\text{c}}I_{\text{s}}\right). \tag{19}$$

Analogous to the previous case, the temperature derivative $\frac{\Delta\text{T}_{r/l,\text{h}/\text{c}}}{\Delta\text{x}_{r/l,\text{h}/\text{c}}}$ defines the temperature difference in the immediate vicinity of the interface temperature $T_{\text{h/c}}$.

There are two heat flow equations corresponding to each of the 7 layers. In addition, the first interface interacts with the heat source and the surrounding air, and the last interface interacts with cold water, leading to a total of 16 equations that keep track of heat flow into and out of the interfaces.

The system is initialized at the same temperature as the surrounding air (288 K). The simulation begins and at each time-step, the 16 heat flow equations are solved simultaneously to determine the 6 interface temperatures, such that there is no accumulation of energy at any interface. The temperatures in the bulk of the system are determined using the Crank Nicholson scheme [40], by solving Eq. (4) numerically. Only the p/n segment has a current term. For the other layers, $j = 0$.

It is customary to define the time-step to be the maximum value $\text{d}x^2/D$, $\text{d}x$ being the difference between the grid points of a segment, and D is the coefficient ($\rho c_{\text{p}}/\lambda$) of the temperature derivative of the heat diffusion equation. Using this criterion, the time step was estimated to be of the order of 10^{-3} s. A time-step of 0.001 s was chosen for further simulations, as it afforded a reasonable accuracy while allowing for a time efficient completion of the simulations.

4.2. Material Properties and Transfer Coefficients

The material properties of the various components of the system are provided in Table 1. The values are obtained from Ref. [41], except for the specific heat capacity of Bi$_2$Te$_3$ semiconductors, which is from Ref. [42]. The Seebeck coefficient and the electrical resistivity were estimated in Ref. [31] from the slope of the open circuit potential and the slope of the polarization curves. The same values were used in this work, i.e. a value of $(300 \pm 4)\,\mu\text{V/K}$ for the Seebeck coefficient and $1.95 \cdot 10^{-5}\,\Omega\text{m}$ for the electrical resistivity.

Table 1: Material Parameters. Area (A), length (l), thermal conductivity (λ), specific heat capacity c_p and density ρ of the materials that constitute the TEG.

Element	$A(m^2)$	l (m)	$\lambda\left(\frac{W}{mK}\right)$	$c_p\left(\frac{J}{kgK}\right)$	$\rho\left(\frac{kg}{m^3}\right)$
Al(1)	6.94×10^{-3}	4.7×10^{-3}	177	910	2.70×10^3
Al(2)	1.60×10^{-3}	5.3×10^{-3}	177	910	2.70×10^3
Al$_2$O$_3$	1.60×10^{-3}	0.8×10^{-3}	35	880	3.96×10^3
Cu	1.60×10^{-3}	0.5×10^{-3}	400	390	8.79×10^3
p/n	2.25×10^{-6}	1.5×10^{-3}	1.6	135	7.64×10^3
Al(3)	6.94×10^{-3}	25×10^{-3}	177	910	2.70×10^3
Air	5.3×10^{-3}	9.4×10^{-3}	3.4×10^{-2}	1.013	8.5×10^{-1}

Other pertinent parameters used in the modeling of the heat flow through the TEG include the convective heat transfer coefficient - from the aluminum hot side to surrounding air, h_{wh}, and from the cold aluminum block to water, h_{cw}. The heat flux into the TEG depends on its distance and angle with respect to the heat source. It also depends on the heat source itself, for example, molten silicon has a different emissivity than molten iron. This aspect can be modeled by tuning the c_{rad} parameter. The ratio of the total area of the TEMs, A_{m}, to the total system cross-sectional area, A, is called the *fractional area* of the TEG, $f_{\text{a}} = A_{\text{m}}/A$. We considered variations in the fractional area by changing A, while keeping A_{m} constant. Explicitly, this means that the areas of Al(1) and Al(3) in Table 1 are varied, while all other areas are kept constant. By changing f_{a}, the amount of air that the system is in contact with also changes, since $A - A_{\text{m}} = A_{\text{air}}$. The parameters explained above were estimated by Børset

6
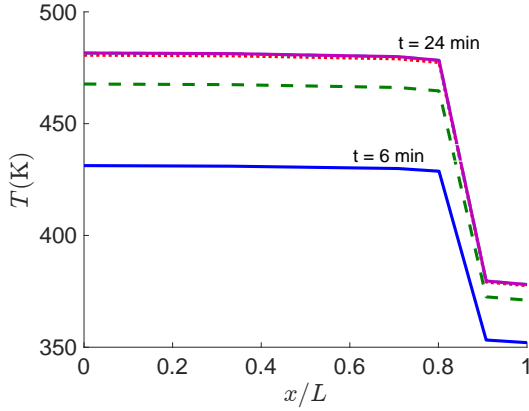
(a) Time evolution of temperature profile through the system with current.
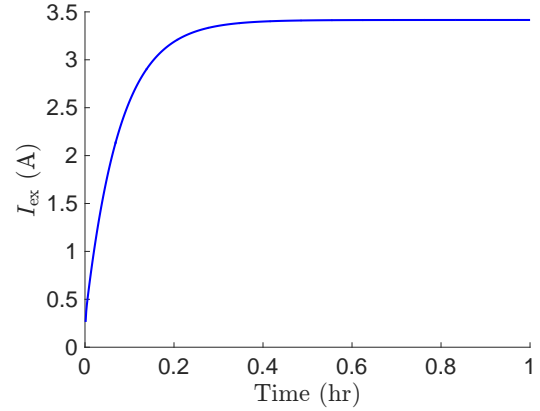
(b) Time evolution of current through the system. It takes 24 minutes for the system to reach steady-state.

Figure 7: In the above plots, the length L is the total length of the system. The length x represents the position of each segment along the thermoelectric device. In these plots, the system was initiated from ambient temperature and was evolved to steady-state. The temperature of the heat source was kept constant at 1673 K.

et al. in Ref. [31] by on-site measurement to be: $h_{cw} = 105$ Wm^{-2}K^{-1}, $h_{wh} = 6$ Wm^{-2}K^{-1}and $f_a = 0.23$.

The coefficient h_{wh} was estimated from an empirical model that uses the average Nusselt number, Nu, for natural convection from a vertical plate. The Nusselt number was found from the correlation Nu = 0.59 Ra$^{1/4}$ where Ra is the Rayleigh number [43]. The coefficient h_{cw} was measured from calculating the heat flow into and out of the system, $UA_{Al}\Delta T_{hav} = A_{Al}h_{cw}(T_{cb} - T_{cw})$. Here ΔT_{hav} is the measured value of the aluminum hot side temperature, T_{cw} is the temperature of cold water and T_{cb} is the temperature of the interface between aluminum oxide and the last aluminum segment.

The TEG is connected to an external circuit, with an external load with resistance $R_{ex} = 3.28$ Ω. Experimentally, it is observed that the maximum power is generated when R_{ex} matches the internal resistance of the p/n semiconductors. R_{ex} is calculated as follows, $R_{ex} = 2N_{pn}r_{p/n}l_{p/n}/A_{p/n}$, where the electrical resistance of the p or the n semiconductors is $r_p = r_n = r_{p/n}$, area $A_p = A_n = A_{p/n}$, and length is $l_p = l_n = l_{p/n}$. The number of pairs of p/n semiconductors in one module is N_{pn}.

5. Results and Discussion

In this section, we will first demonstrate that the dynamic model reproduces the steady-state results (Sec. 5.1). We will then compare the results from a mathematical model of time change in temperature of the TEG to on-site experiments under transient operation conditions (Sec. 5.2) and show that the model reproduces the experimental results.

We will then use the model to evaluate the potential to enhance the performance of the TEG by changing its position and cooling capacity, while staying within the constraints imposed by the materials (Sec. 5.3). Next, the potential to

enhance power output by changing its design, given that the TEG is located at a fixed position is investigated (Sec. 5.4). Finally, we explore the possibility of simultaneously changing the design and the position of the TEG. Venues to improve the performance of TEGs that operate under transient conditions are suggested (Sec. 5.5).

In this work, we have used bismuth-telluride (Bi-Te) type semiconductors as example. However, we expect the findings and behavior of the TEG to be generally valid for similar semiconductors such as BiSnTe-based or PbSe-based TEMs. The choice of semiconductor will mainly influence the magnitude of the maximum peak power density that can be obtained.

5.1. Validating the transient model

To validate the mathematical model and the numerical implementation, a simulation was performed where the TEG was initiated from room temperature (288 K), and was evolved towards steady-state. Keeping the temperature of the heat source, T_m at a constant value of 1673 K, steady-state was obtained when the temperature profile remained constant with time, and there was no accumulation of heat at any interface, implying that $\dot{Q}_i^{in} = \dot{Q}_i^{out}$.

The steady-state temperature profile resulting from the dynamic model was compared with the profile obtained by solving a set of algebraic equations similar to Ref. [31]. The temperature profile from the dynamic model converged within ± 1 K of the steady-state results after about 24 minutes. We let the system run for a total time of 2 hours to confirm that the temperature did not overshoot the steady-state value.

At the start of the simulation, all layers are at the same temperature. As one side of the system heats up, and the other

7
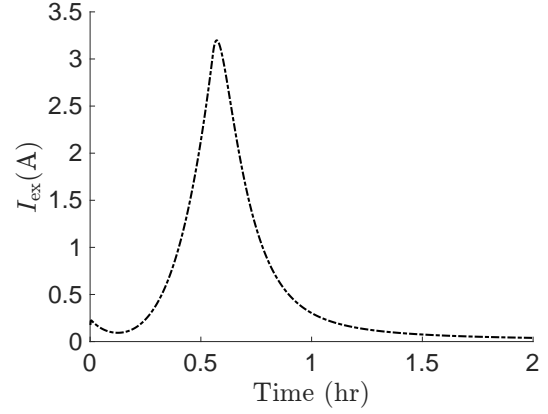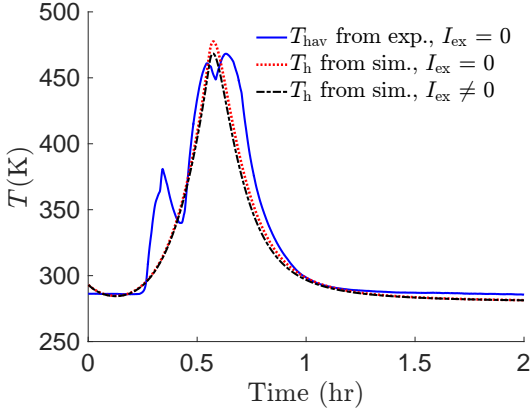
(a) Time evolution of average temperature of the heating block, T_{hav}, from on-site experiments (no current passes trough the system), and T_h from the simulation, for the base TEG design, i.e., $f_a = 0.23$, for one cycle of the casting process, when current passes through the system (black dash-dot line) and with no current passing through the system (red dashed line).

(b) Time evolution of current through the system under varying temperature of the silicon melt corresponding to Fig. 8a, for the base TEG design, i.e., $f_a = 0.23$.

Figure 8: Time evolution of hot side temperature and the current generated when modeling a varying temperature of the silicon melt.

is maintained at a lower temperature, the temperature gradient gradually increases. Figure 7a shows that the system heats up relatively quickly in the beginning, and then slowly converges to the steady-state solution.

The temperature gradient induces an electric potential difference, resulting in the generation of current and the system cools down as heat is converted into electrical power in the process. The largest temperature drop occurs across the p/n segment where current is being generated. Fig. 7b, shows the time evolution of current in the p/n semiconductors. It takes about 24 minutes for the interface temperatures and the current to reach their peak values. The figure shows that in the first 10 minutes, the magnitude of current increases fairly quickly, in tune with the temperature jump across the p/n segment.

5.2. Modeling the silicon casting process

The equations that govern the temperature of the silicon melt were presented in Sec. 3.2. By combining the model of the silicon melt with the model of the TEG, we can compare the time evolution of the temperature of the interface facing the heat source, T_{sh} (see Fig.5), with the average temperature of the heating block, T_{hav}, from on-site measurements. We used the following parameters: $c_{rad}^0 = 0.036$ and $f = 200$ m^2. The temperature measurements in Fig. 8a were performed with no current passing through the system ($I_{ex} = 0$) to isolate the effect of the TEG heating up. It was shown in previous work that the mathematical model captures accurately the current and power generated by the TEG (see Fig. 5 in Ref. [31]).

Figure 8a displays a good qualitative agreement between the model and the experiments. The experimental temperature profile is more complex than the one from the model, however, the mathematical model captures key aspects of the experiments such as the peak temperature and the width of the curve. For comparison, we have included in Fig. 8a the hot side temperatures from the simulations when no current passes through the system (red-dashed line) and when current passes through the system (black dash-dot line). The figure shows that the passing of current through the system influences mainly the peak temperature when the current is largest. The peak temperature decreases by ~9 K when current passes through the system, however, the drop in temperature increases with larger electrical currents. Figure 8b shows the current generated over one casting period as predicted by the model. The current follows a periodic profile similar to the surface temperature, as shown in Fig. 8a. We define the peak power density, P_{peak} to be the maximum power per area produced during one casting cycle, and we define the average power density P_{av} as

$$P_{av} = \frac{1}{A\tau} \int_0^\tau P(t)\mathrm{d}t, \tag{20}$$

where $\tau = 2$ hours, is the duration of one casting period. For the base case of the transient model ($c_{rad} = 0.036$), P_{peak}, was found to be 134 W/m^2, and P_{av} was 12 W/m^2. The average power generated in the silicon production process is only 9% of P_{peak}, as the peak value of the power is only maintained for a couple of minutes.

8

5.3. Enhancing the performance of the TEG by changing its position and cooling capacity

The amount of heat transferred to the TEG depends on its distance and angle with respect to the heat source. It also depends on the heat source itself. The location of the TEG influences mainly its view factor, which is proportional to the radiative heat flux. This aspect was modeled by tuning the c_{rad} parameter. It is also likely that the temperature of the surrounding air increases slightly when the TEG is moved closer to the carousel, but this has been neglected in the present analysis. When the incoming radiation to the thermoelectric device increases, the TEG should be equipped to withstand the resulting high temperatures. This can be achieved by improving the cooling capacity of the TEG. In practice, this can be accomplished by:

1. Increasing the flow rate of water to enhance the turbulence, and consequently the cold-side heat transfer coefficient.
2. Doubling or quadrupling the contact area at the cold-side of the TEG, e.g. by covering more over the cold-side of the TEG with cooling pipes or by using fins inside the cooling channels to extend the cold-side heat transfer area.

All of these changes influence the model similarly and can thus be emulated by doubling or quadrupling the convective heat transfer coefficient between aluminum and water (h_{cw}). The value of the fractional area in this case is $f_a = 0.23$.

The hot side of the p/n semiconductors in the TEG begins to deteriorate at $T_h = 653$ K, and the cold side begins to deteriorate at $T_c = 433$ K [31], these are the material temperature limits of the TEG. Figures 9a and 9b show the peak temperature T_{peak}, reached by the hot side and the cold side of the TEG. With a lower cooling capacity, the cold side of the TEG reaches the material stability limit first. As the cooling capacity is increased, higher values of c_{rad} can prevail i.e. the TEG can be moved closer to the heat source without harming the device.

Table 2 summarizes the maximum power density and maximum average power density that can be generated for three different cooling capacities before either the hot side or the cold side of the TEG begin to deteriorate. One can see that the relative gain in power density is diminishing with increasing h_{cw}. When h_{cw} is increased from 105 to 210 W/m²K⁻¹, P_{peak} increases by 187%, and when h_{cw} changes from 210 to 420 W/m²K⁻¹, P_{peak} increases by only another 46%.

For all the three investigated cooling capacities, the time average power density generated during one casting period is only 7-10% of the maximum power density generated. Even so, increasing the cooling capacity is a viable option since it allows the TEG to be placed closer to the silicon melt. In the present design, the aluminum cold side is cooled with the help of tap water flowing through copper pipes embedded in the plate, and water is an available resource. Table 2 shows that by quadrupling the cooling capacity, there is a potential to increase both the peak power density and the average power density generated by the TEG, provided that the location of the TEG can be changed simultaneously.

Table 2: Peak power density and average power density generated under physically admissible conditions for different values of h_{cw}. For each value of h_{cw}, the power density was found as a function of c_{rad} and h_{cw}.

| $h_{cw} \left(\text{Wm}^{-2}\text{K}^{-1}\right)$	c_{rad}/c_{rad}^0	$P_{peak} \left(\text{W/m}^2\right)$	$P_{av} \left(\text{W/m}^2\right)$
105	1.7	325	30
210	2.6	932	77
420	3.0	1370	108

5.4. Enhancing the performance of the TEG by changing its design at fixed location

If the location of the TEG in the silicon casting plant is predetermined, the design of the TEG can be altered to achieve a higher temperature gradient across the semiconductors, thereby increasing the power output. This can be achieved by reducing the fractional area f_a. The fractional area can be changed by keeping A_m constant while varying A. By decreasing f_a, the area of aluminum plate increases while the number of TEMs which consists of p/n semiconductors and air remains constant. This implies that a smaller fraction of heat is transported through the TEM as A grows, because decreasing f_a increases the fraction of air, and air has poor heat transfer properties. Thus, the temperature on the hot side increases, and the temperature at the cold side of the TEG decreases, as f_a decreases. In order to probe this dependence, we plotted T_h and T_c as functions of f_a for given values of h_{cw} and c_{rad}. The result is plotted for the base value of c_{rad} in Fig. 10a.

In agreement with the trends observed by Børset et al. [31], the maximum power density increases with decreasing fractional area as shown in Fig. 10c. The average power density also continues to increase with decreasing fractional area in Fig. 10d. In this scenario, the effect of changing the cooling capacity is not very pronounced, with the average power density changing by only 4 W/m² by quadrupling the cooling capacity.

Since the TEM transfers heat more efficiently than air, a smaller amount of heat is transferred from the hot side to the cold side when the fractional area decreases. Therefore it takes a longer time for the hot side of the TEG to cool down with a smaller fractional area, once the temperature of the heat source is decreasing. This is reflected by a steeper temperature gradient as shown in Fig. 10a as well as a broadening of the profile of the time dependent current generated by the TEG normalized by the peak value, as shown in Fig. 10b. The broadening of the current profile implies that the average power density increases more than the peak power density as the fractional area decreases.

9
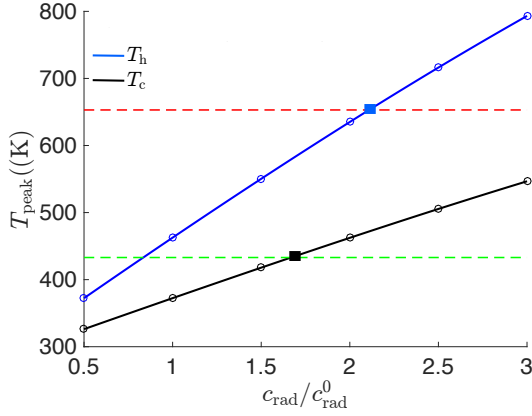
(a) Peak temperature of the hot side of the TEG, T_h and the cold side T_c for $h_{cw} = 105$ Wm^{-2}K^{-1}. The dashed lines represents the material stability limits for the cold-side and the hot-side. Squares indicate the c_{rad} value where the material constraint is reached. The circles are simulation points.
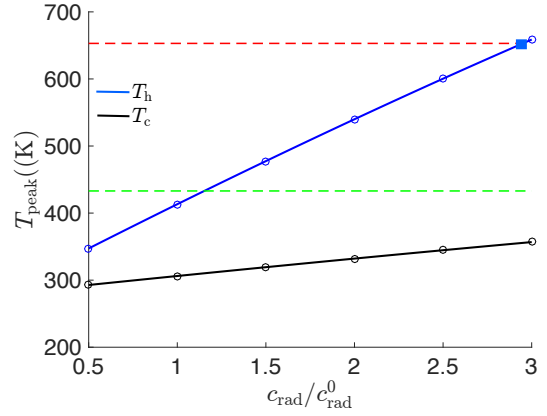
(b) Peak temperature of the hot side of the TEG, T_h and the cold side T_c for $h_{cw} = 420$ Wm^{-2}K^{-1}. The dashed lines represents the material stability limits for the cold-side and the hot-side. Squares indicate the c_{rad} value where the material constraint is reached. The circles are simulation points.

Figure 9: Peak temperatures at the hot-side and the cold-side of the TEG with two different cooling capacities.

5.5. Enhancing the performance of the TEG by simultaneously changing its design and location

In this section, we shall explore the potential to further enhance the performance by simultaneously changing the design and the position of the TEG. While reducing the fractional area when the TEG is at a fixed position improves its performance, it does not necessarily improve the TEG's performance when the location is changed simultaneously. For a given h_{cw} and f_a, the *optimal* position of the TEG corresponds to the location where the TEG can be placed as close as possible to the silicon melt without exceeding the material stability limits of the p/n semiconductors. The resulting peak and average power density are plotted in Figs. 11a and 11b. These figures represent the best case performance of the TEG for a given design and cooling capacity.

We can see that the location of the peak power density and the average power density shifts towards higher fractional areas with a higher cooling capacity. With a higher fractional area, a larger heat flux can pass through the TEMs with the same temperature gradient, and a higher power density can thus be generated. Both the peak power density and the average power densities exhibit maxima as functions of the fractional area for all cooling capacities that have been studied. These peaks correspond to a fractional area where the hot-side and and cold-side break down for the same c_{rad} - that is, the c_{rad} for which the hot-side peak temperature is 653 K, while the cold-side peak temperature is 453 K. Beyond the maxima, the aluminum cold-side reaches its stability limit first. This limits how high the aluminum hot-side temperature can become, therefore restricting the power output.

The optimal combination of f_a and c_{rad} depends strongly on the cooling capacity of the system. For higher cooling capacities, the hot side of the TEG reaches the stability limit first. For this case, it is beneficial to move the TEG towards the silicon melt to increase the temperature gradient across the TEG instead of reducing the fractional area.

Figure 11c shows that the ratio of the average to the peak power density increases with smaller fractional areas in the region $f_a \geq 0.3$. In this region, the hot-side and the cold-side temperatures begin to flatten out. For high fractional areas, the difference between the hot side-temperature and the cold-side, and likewise, the difference between the peak power density and the average power density in the tail end is small, so the ratio between the peak power density and the average power density is almost constant, but shows a slight increase for $h_{cw} = 105$ W/m^{2}K^{-1}.

Table 3 summarizes the maximum power density and the average power density generated for different cooling capacities, given that both the optimum design and location of the TEG have been identified. As discussed in section 5.3, with a lower cooling capacity, the aluminum cold side reaches the material stability limit first. The TEG can be moved closer to the silicon melt with higher cooling capacities. The average power density is in all investigated cases about 7-10% of the peak power density. The maximum attainable power density was found to be 1971 W/m^2.

For the optimal position of the TEG, quadrupling the convective heat transfer coefficient h_{cw} from the base value of 105 W/m^{2}K^{-1} increases the maximum power output by 385%, while the average power density increases by 217%. Since the ratio of the average power density to the peak power density was between 7-10% in all investigated cases, the most effi-
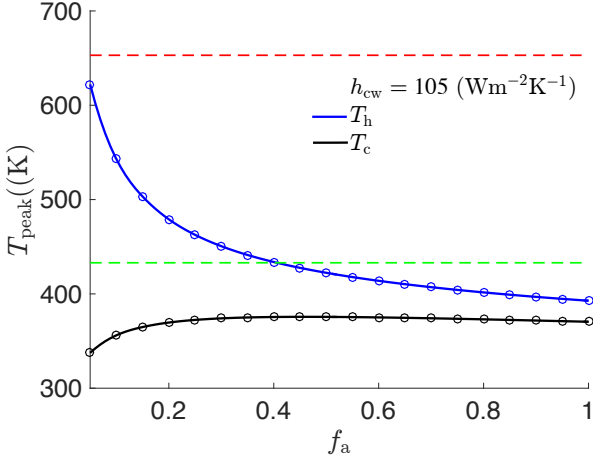
(a) Peak temperature of the hot side of the TEG, T_h and the cold side T_c, for $h_{cw} = 105$ (Wm^{-2}K^{-1}), plotted as a function of f_a at constant $c_{rad}/c_{rad}^0 = 1$. The dashed lines indicate the temperatures at which the hot side and the cold side of the TEG begin to deteriorate. The circles are simulation points.
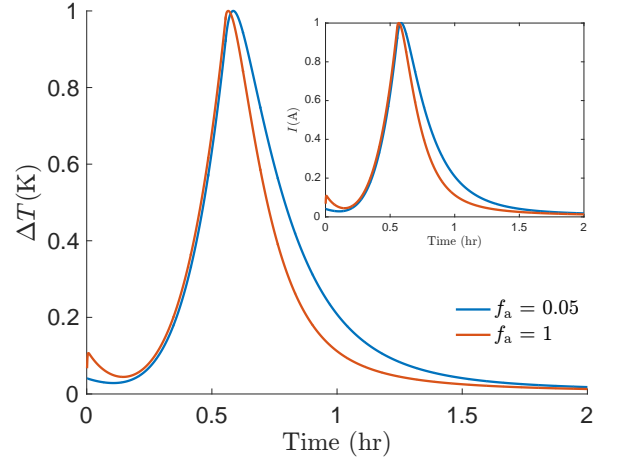
(b) The temperature difference and current (inset plot), both normalized by the peak, for two different values of f_a, and for base $c_{rad} = 0.036$, and $h_{cw} = 105$ Wm^{-2}K^{-1}. For a small fractional area, the width of the curve is broader.
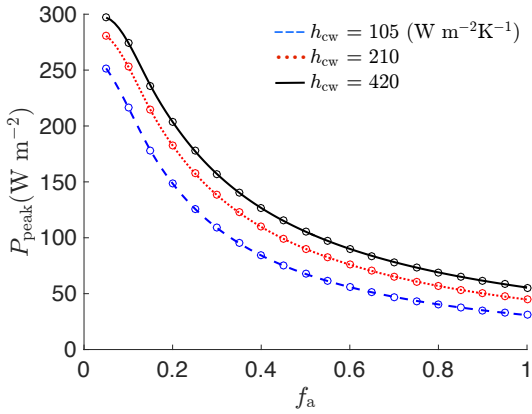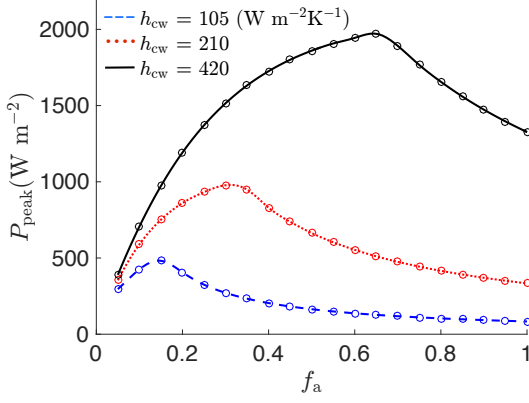
(c) Maximum power density generated as a function of fractional area, for base case c_{rad}, for different cooling capacities. The circles represent simulation points.
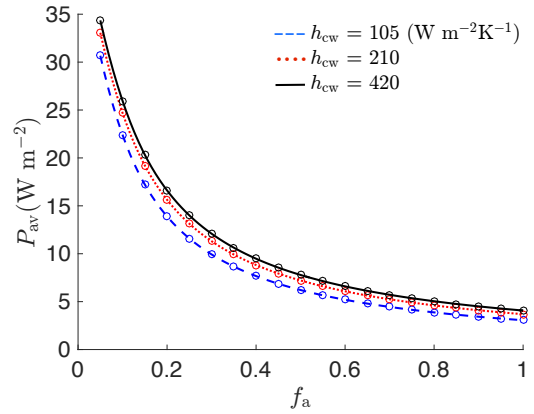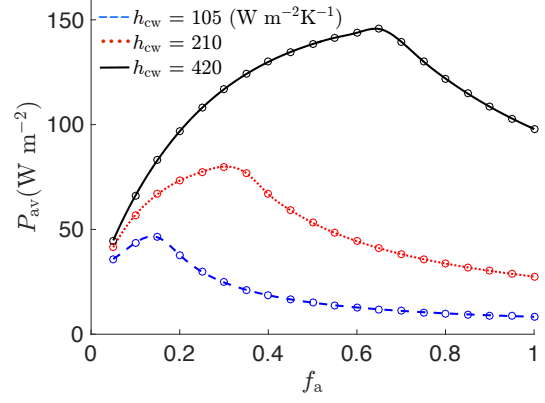
(d) Power density averaged over one period as a function of the fractional area, for base case c_{rad}, as a function of f_a for different cooling capacities. The circles represent simulation points.
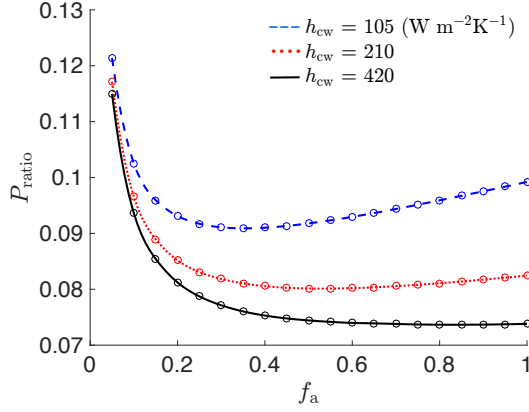
Figure 10: Performance and characteristics of the TEG for changes in the fractional area.

(a) Maximum power density generated as a function of f_a, for optimized c_{rad}, for different cooling capacities. The circles represent simulation points.

(b) Power density averaged over one period as a function of f_a, for optimized c_{rad}, for different cooling capacities. The circles represent simulation points.

(c) Ratio of maximum power density to average power density as a function of f_a, for optimized c_{rad}, for different cooling capacities. The circles represent simulation points.

Figure 11: Evaluating the optimal performance of the TEG as a function of the fractional area with simultaneous changes in its design and location.

Table 3: The peak power density and the average power densities generated under physically admissible conditions for different values of h_{cw}. For each value of h_{cw}, the power density was found as a function of f_a. The optimum values of c_{rad} corresponding to each f_a are reported.

h_{cw} (Wm-2K^{-1})	c_{rad}/c_{rad}^0	f_a	P_{peak}(W/m^2)	P_{av} (W/m^2)
105	1.7	0.15	406	46
210	2.8	0.30	977	80
420	5.3	0.65	1971	146

607 effect on the final power output. A possible venue for further in-
608 creasing the performance of TEGs that operate under dynamic
609 conditions could be to use the cooling capacity as control vari-
610 able.

601 cient way to increase the average power density generated by
602 the TEG is to increase the peak power density. However, the
603 magnitude of the peak power density is limited by material con-
604 straints. Since the design of the TEG influences the power ratio
605 (Fig. 11c), future work should be performed to find avenues to
606 alter the TEG design or operation conditions to investigate its

12

6. Conclusion

In this work, we have investigated the potential of using thermoelectric generators (TEGs) to recover waste heat in a silicon production plant, where the average temperature of the heat source varies periodically with time.

In a silicon production plant, silicon is cast periodically in batches lasting for about two hours. A TEG with a 0.5 m × 0.5 m surface area and 6 × 6 bismuth-telluride thermoelectric modules (TEMs) was placed at a fixed position in the silicon production plant. Key parameters like the power density generated by the TEG and the temperature of the heating block were measured. We found that the power density follows a periodic profile where a peak power density was reached after about 30 minutes, before the power started to decrease.

Next, we developed transient mathematical models of the TEG and the silicon melt that were capable of reproducing the experimental results, both at steady-state and under transient conditions. We then used the model to explore the potential of the TEG to recover waste heat under the transient operation conditions of a silicon production plant. We found that the power density generated by the TEG depended on several parameters, such as the position and angle of the TEG relative to the heat source, the cooling capacity, and the design of the TEG. For all the cases we investigated, the average power density generated during one casting period was only 7% - 10% of the peak power density.

The temperatures of the cold or the hot side of the p/n semiconductors at the time when the peak power density is reached determine how close to the silicon melt the TEG can be placed. For low cooling capacities, the temperature at the cold side of the p/n semiconductor was the limiting factor, but for higher cooling capacities, the temperature at the hot side was found to be the limiting factor.

By bringing the TEG closer to the heat source, we found that the average power density and the peak power density increased. However, bringing the TEG closer to the heat source demanded that the cooling capacity of the TEG was improved in comparison to the reference case, so that the TEG could withstand the resulting high temperatures. When the heat transfer coefficient at the cold side of the TEG, h_{cw}, was increased from 105 to 210 $Wm^{-2}K^{-1}$, the maximum attainable peak power density increased by 187%, and when h_{cw} was further increased from 210 to 420 $Wm^{-2}K^{-1}$, the corresponding the peak power density increased by another 46%.

A typical design parameter of TEGs is the fractional area, which is defined as the ratio of the total area of the TEMs to the total system cross-sectional area. In a scenario where the location of the TEG has been fixed beforehand, we found that the power output could be increased by decreasing the fractional area. This is also beneficial from an economic perspective, since less modules can be used. By decreasing the fractional area, the temperature gradient through the TEG increased, but the heat flux decreased. This resulted in the broadening of the current profile as a function of time.

For a situation in which both the position of the TEG and the fractional area were allowed to change and the TEG was positioned as close to the heat source as possible without exceeding the material constraint, we found that there was an optimum fractional area which depended on the cooling capacity. The peak power density and the average power density reached maximum values beyond which the power as a function of the fractional area declined. We found that beyond the maxima, the aluminum cold-side reached the material stability limit before the aluminum hot-side. This limits the reachable hot-side temperature, thus restricting the power output.

It was possible to obtain a power density density as high as 1971 Wm^{-2} under optimum conditions, however, the average power density produced during a casting period was only 146 Wm^{-2}.

The temperature constraints of the p/n semiconductors in the bismuth-telluride thermoelectric elements limit the maximum achievable power density. The temperature of the TEG is highest when maximum power is being produced, which then limits the maximum attainable power. Future work to enhance the performance of TEGs operating under transient environment of a metal casting plant should therefore aim at increasing the ratio of the average power density to the maximum power density. This could possibly be achieved by controlling the cooling of the TEG in such a way that the temperature difference of the TEG is maintained when the heat source temperature begins to decrease, or alternatively by changing the design of the TEG.

7. Acknowledgements

References

[1] I. Z. Bribian, A. V. Capilla, and A. A. Uson. Life cycle assessment of building materials: Comparative analysis of energy and environmental impacts and evaluation of the eco-efficiency improvement potential. *Build. Environ.*, 46 (5):1133 – 1140, 2011.

[2] A. Johari, S. I. Ahmed, H. Hashim, H. Alkali, and M. Ramli. Economic and environmental benefits of landfill gas from municipal solid waste in malaysia. *Renew. Sustainable Energy Rev.*, 16(5):2907 – 2912, 2012.

[3] S. Chalasani and J. M. Conrad. A survey of energy harvesting sources for embedded systems. In *IEEE SoutheastCon 2008*, pages 442–447, 2008.

[4] D. N. Kossyvakis, G. D. Voutsinas, and E. V. Hristoforou. Experimental analysis and performance evaluation

of a tandem photovoltaicâĂŞthermoelectric hybrid system. *Energy Conversion and Management*, 117:490 – 500, 2016.

[5] M. Chen, L. A. Rosendahl, T. J. Condra, and J. K. Pedersen. Numerical modeling of thermoelectric generators with varying material properties in a circuit simulator. *IEEE Trans. Energy Convers.*, 24(1):112–124, 2009.

[6] T. Caillat, J. P. Fleurial, G. J. Snyder, Zoltan A., Zoltan D., and Borshchevsky A. A new high efficiency segmented thermoelectric unicouple. In *34th Intersociety Energy Conversion Engineering Conference*, 1999.

[7] R. McCarty. Thermoelectric power generator design for maximum power: It's all about ZT. *J. Electron. Mater.*, 42(7):1504–1508, 2012.

[8] S. LeBlanc, S. K. Yee, M. L. Scullin, C. Dames, and K. E. Goodson. Material and manufacturing cost considerations for thermoelectrics. *Renew. Sust. Energy Rev.*, 32:313–327, 2014.

[9] S. K. Yee, S. LeBlanc, K. E. Goodson, and C. Dames. \$ per w metrics for thermoelectric power generation: Beyond ZT. *Energy Environ. Sci.*, 6(9):2561–2571, 2013.

[10] C. Liu, P. Chen, and K. Li. A 500 W low-temperature thermoelectric generator: Design and experimental study. *Int. J. Hydrogen Energy*, 39(28):15497 – 15505, 2014.

[11] C. Liu, X. Pan, X. Zheng, Y. Yan, and W. Li. An experimental study of a novel prototype for two-stage thermoelectric generator from vehicle exhaust. *J. Energy Inst.*, 89(2):271–281, 2016.

[12] X. Niu, J. Yu, and S. Wang. Experimental study on low-temperature waste heat thermoelectric generator. *J. of Power Sources*, 188(2):621–626, 2009.

[13] CT. Hsu, GY. Huang, HS. Chu, B. Yu, and DJ. Yao. Experiments and simulations on low-temperature waste heat harvesting system by thermoelectric power generators. *Appl. Energy*, 88(4):1291–1297, 2011.

[14] R. O. Suzuki and D. Tanaka. Mathematic simulation on thermoelectric power generation with cylindrical multi-tubes. *J. of Power Sources*, 124(1):293–298, 2003.

[15] R. O. Suzuki and D. Tanaka. Mathematic simulation on power generation by roll cake type of thermoelectric tubes. *J. of Power Sources*, 132(1-2):266 – 274, 2004.

[16] G. Chen. Theoretical efficiency of solar thermoelectric energy generators. *J. Appl. Phys.*, 109(10), 2011.

[17] B. V. K. Reddy, M. Barry, J. Li, and M. K. Chyu. Mathematical modeling and numerical characterization of composite thermoelectric devices. *Int. J. Therm. Sci.*, 67:53 – 63, 2013.

[18] Y. Shi, Z. Zhu, Y. Deng, W. Zhu, X. Chen, and Y. Zhao. A real-sized three-dimensional numerical model of thermoelectric generators at a given thermal input and matched load resistance. *Energy Convers. and Manage*, 101:713 – 720, 2015.

[19] N. R. Kristiansen, G. J. Snyder, H. K. Nielsen, and L. Rosendahl. Waste heat recovery from a marine waste incinerator using a thermoelectric generator. *J. Electron. Mater.*, 41(6):1024–1029, 2012.

[20] S. Kumar, S. D. Heister, X. Xu, J. R. Salvador, and G. P.
Meisner. Thermoelectric generators for automotive waste heat recovery systems Part I: Numerical modeling and baseline model analysis. *J. Electron. Mater.*, 42(4):665–674, 2013.

[21] S. Yu, Q. Du, H. Diao, G. Shu, and K. Jiao. Effect of vehicle driving conditions on the performance of thermoelectric generator. *Energy Convers. and Manage*, 96:363 – 376, 2015.

[22] N. Q. Nguyen and K. V. Pochiraju. Behavior of thermoelectric generators exposed to transient heat sources. *Appl. Therm. Eng.*, 51(1-2):1–9, 2013.

[23] A. Montecucco and A. R. Knox. Accurate simulation of thermoelectric power generating systems. *Appl. Energy*, 118:166–172, 2014.

[24] A. Montecucco, J. R. Buckle, and A. R. Knox. Solution to the 1-D unsteady heat conduction equation with internal joule heat generation for thermoelectric devices. *Appl. Therm. Eng.*, 35(1):177–184, 2012.

[25] O. Yamashita, H. Odahara, and K. Satou. Energy conversion efficiency of a thermoelectric generator under the periodically alternating temperature gradients. *J. Appl. Phys.*, 101(2), 2007.

[26] D. T. Crane, C. R. Koripella, and V. Jovovic. Validating steady-state and transient modeling tools for high-power-density thermoelectric generators. *J. Electron. Mater.*, 41, 2012.

[27] D. T. Crane. An introduction to system-level, steady-state and transient modeling and optimization of high-power-density thermoelectric generator devices made of segmented thermoelectric elements. *J. Electron. Mater.*, 40(5):561–569, 2010.

[28] A. Paraskevas and E. Koutroulis. A simple maximum power point tracker for thermoelectric generators. *Energy Convers. and Manage*, 108:355–365, 2016.

[29] T. Kuroki, K. Kabeya, K. Makino, T. Kajihara, H. Kaibe, Hi Hachiuma, H. Matsuno, and A. Fujibayashi. Thermoelectric generation using waste heat in steel works. *J. Electron. Mater.*, 43(6):2405–2410, 2014.

[30] L. Chen and J. Lee. Efficiency enhancement of an industrial-scale thermoelectric generator system by periodically inputting thermal power. *Energy Convers. and Manage*, 119:75 – 80, 2016.

[31] M. T. Børset, Ø. Wilhelmsen, S. Kjelstrup, and O. S. Burheim. Exploring the potential for waste heat recovery during metal casting with thermoelectric generators: On-site experiments and mathematical modeling. *Energy*, 2016. doi: http://dx.doi.org/10.1016/j.energy.2016.10.109.

[32] S. Kjelstrup and D. Bedeaux. *Non-Equilibrium Thermodynamics of Heterogeneous Systems*. World Scientific, 2008.

[33] Ø. Wilhelmsen, D. Bedeaux, and S. Kjelstrup. Heat and mass transfer through interfaces of nanosized bubbles/droplets: the influence of interface curvature. *Phys. Chem. Chem. Phys.*, 16:10573–10586, 2014. doi: 10.1039/C4CP00607K.

[34] Ø. Wilhelmsen, T. T. Trinh, S. Kjelstrup, T. S. van Erp,

and D. Bedeaux. Heat and mass transfer across interfaces in complex nanogeometries. *Phys. Rev. Lett.*, 114:065901, Feb 2015. doi: 10.1103/PhysRevLett.114.065901.

[35] Ø. Wilhelmsen, T. T. Trinh, S. Kjelstrup, and D. Bedeaux. Influence of curvature on the transfer coefficients for evaporation and condensation of lennard-jones fluid from square-gradient theory and nonequilibrium molecular dynamics. *J. Phys. Chem. C*, 119(15):8160–8173, 2015. doi: 10.1021/acs.jpcc.5b00615.

[36] Ø. Wilhelmsen, T. T. Trinh, A. Lervik, V. K. Badam, S. Kjelstrup, and D. Bedeaux. Coherent description of transport across the water interface: From nanodroplets to climate models. *Phys. Rev. E*, 93:032801, Mar 2016. doi: 10.1103/PhysRevE.93.032801.

[37] R. Rurali, L. Colombo, X. Cartoixa, Ø. Wilhelmsen, T. T. Trinh, D. Bedeaux, and S. Kjelstrup. Heat transport through a solid-solid junction: the interface as an autonomous thermodynamic system. *Phys. Chem. Chem. Phys.*, 18:13741–13745, 2016. doi: 10.1039/C6CP01872F.

[38] WK. Rhim and K. Ohsaka. Thermophysical properties measurement of molten silicon by high-temperature electrostatic levitator: density, volume expansion, specific heat capacity, emissivity, surface tension and viscosity. *J. Cryt. Growth*, 208(1-4):313–321, 2000.

[39] Silicon properties. http://www.janis.com/Libraries/Window_Transmissions/Silicon_Si_TransmissionCurveDataSheet.sflb.ashx.

[40] W. H. Press, S. A. Teukolsky, W. T. Vetterling, and B. P. Flannery. *Numerical recipes in C*, volume 2. Cambridge university press Cambridge, 1996.

[41] Material properties. http://www.engineeringtoolbox.com.

[42] N. P. Gorbachuk and V. R. Sidorko. Heat capacity and enthalpy of bi2si3 and bi2te3 in the temperature range 58-1012 k. *Powder Metall. Met. C+*, 43(5):284–290, 2004.

[43] Y. A. Çegal. *Heat and Mass Transfer: A Practical Approach, 3rd Edition*. McGrawHill, New York, 2006.